



# Additive manufacturing of dense components in beta-titanium alloys with crystallographic texture from a mixture of pure metallic element powders

Takeshi Nagase<sup>a,b</sup>, Takao Hori<sup>b</sup>, Mitsuharu Todai<sup>c</sup>, Shi-Hai Sun<sup>b</sup>, Takayoshi Nakano<sup>b,\*</sup>

<sup>a</sup> Research Center for Ultra-High Voltage Electron Microscopy, Osaka University, 7-1, Mihogaoka, Ibaraki, Osaka 567-0047, Japan

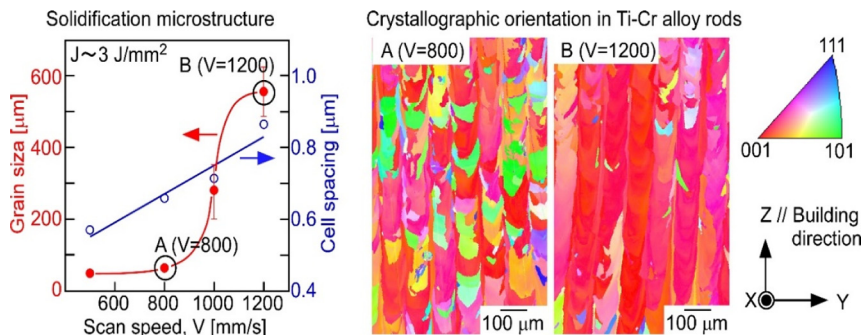
<sup>b</sup> Division of Materials and Manufacturing Science, Graduate School of Engineering, Osaka University, 2-1, Yamadaoka, Suita, Osaka 565-0871, Japan

<sup>c</sup> Department of Environmental Materials Engineering, National Institute of Technology, Niihama College, 7-1, Yakumocho, Niihama, Ehime 792-8580, Japan

## HIGHLIGHTS

- Selective laser melting using a mixture of pure element powders was investigated.
- Dense components in Ti-X (X = Cr, Nb, Mo, Ta) alloys were fabricated.
- Ti-Cr alloy specimens exhibit a single  $\beta$ -Ti phase without any non-molten powders.
- Ti-Cr alloy specimens show  $\{001\}<100>$  crystallographic texture.
- The crystallographic texture formation during selective laser melting was analyzed.

## GRAPHICAL ABSTRACT



## ARTICLE INFO

### Article history:

Received 2 February 2019

Received in revised form 18 March 2019

Accepted 28 March 2019

Available online 31 March 2019

### Keywords:

Additive manufacturing (AM)

Selective laser melting (SLM)

Titanium alloys

Solidification

Microstructure

Texture

## ABSTRACT

The fabrication of dense components composed of Ti-based alloys, i.e., Ti-X (X = Cr, Nb, Mo, Ta) alloys, from a mixture of pure elemental powders was achieved using selective laser melting (SLM) process. The Ti-Cr alloys comprise  $\beta$ -Ti single-phase components without any non-molten particles and macroscopic defects. The crystallographic texture of these  $\beta$ -Ti-Cr alloys can be controlled effectively by optimizing the build parameters. The development of  $\{001\}<100>$  crystallographic orientation during the SLM process is discussed based on the solidification process focusing on the columnar cell growth in the melt pool. These results demonstrate the possibility of fabricating the Ti-based alloy components with well-developed crystallographic texture from the mixture of pure elemental powders using the process of SLM.

© 2019 The Authors. Published by Elsevier Ltd. This is an open access article under the CC BY license (<http://creativecommons.org/licenses/by/4.0/>).

## 1. Introduction

Titanium (Ti) alloys are regarded as promising materials in diverse areas such as automobiles, aircrafts, marine engineering, chemical engineering, and biological engineering due to their features of low density, high strength, good ductility, significant corrosion resistance, and

\* Corresponding author.

E-mail address: [nakano@mat.eng.osaka-u.ac.jp](mailto:nakano@mat.eng.osaka-u.ac.jp) (T. Nakano).

superior biocompatibility [1,2]. Although Ti is the fourth most abundant metallic element in the earth's crust and its alloy has superior properties as mentioned above, the usage of the Ti has been somewhat limited because of the relatively high cost associated with the fabrication process, arising due to the significantly high reactivity of Ti in the molten state. Recently, additive manufacturing (AM) has attracted considerable interest in noble metal manufacturing [3–14]. AM does not require expensive molds or dies, thus avoiding the possible contamination from them and reducing the cost for small runs. Furthermore, AM enables the production of complex geometries, which cannot be fabricated using conventional manufacturing techniques such as casting, powder processing, and/or plasticity processing. Therefore, the application of AM is strongly desired for pure Ti and Ti alloys.

Selective laser melting (SLM) is an AM process in which shapes with complex geometries are produced by selectively melting consecutive layers of a powder with a high-power laser beam. In SLM, a laser locally melts successive layers of the powder, which are then rapidly solidified, resulting in a particular solidification microstructure. One of the most important challenges in SLM is the fabrication of highly dense metallic alloy components in the desired composition from a mixture of pure elements. Starting from the cheap and free designing mixed powders of pure metals or alloys and combining the fabrication ability of complex structure for SLM, it opens up possibilities for the development of new fabrication processes for Ti and Ti alloys with advanced properties. Bulk Ti-6Al-4V parts were produced from a powder mixture of elemental Ti, Al, and V [15]; a homogeneous melt mixing was achieved and no significant difference was observed in the mechanical properties of the products obtained from the mixture of pure elements and from the pre-alloy powders. SLM processes were also reported for a mixture of pure Ti and V [16] and Ti and Mo [16,17]. A compositional gradient, from elemental Ti to Ti-25 wt% V or Ti-25 wt% Mo, has been achieved within a length of ~25 mm [16]. Ti-Mo alloys with compositions varying from 0 to 19 wt% Mo were produced by variable powder feed rate laser cladding and characterized by suitable micro-characterization methods [18]. Using SLM, Vrancken and Humbeeck et al. developed an advanced  $\beta$ -Ti composite [18]. SLM of a mixture of Ti-6Al-4 V-Extra Low Interstitial (ELI) and pure Mo resulted in a microstructure consisting of a  $\beta$ -Ti matrix with randomly dispersed pure Mo particles. All the alloys showed a mixture of  $\alpha$  (hcp),  $\beta$  (BCC),  $\alpha'$  (hcp martensite), and  $\alpha''$  (orthorhombic martensite) phases, but the formation of a single  $\beta$  phase was not reported. Furthermore, attempts were made to prepare Ti-Nb [19] and Ti-Ta-Zr [20] alloys from mixtures of pure element powders for biomedical applications. The preliminary work required for conducting an SLM of a mixture of Ti-Cr and Ti-Nb alloys was also reported [21].

The other challenging aspect in SLM is the control of the crystallographic orientation structure. In the literature available on the SLM of Ti-6Al-4 V alloys, the crystallographic texture was reported to be dependent on the scanning strategy [22,23]. The formation of elongated grains, several hundred micrometers long, due to the partial remelting of the previous layers, was reported in Ti-6Al-4V alloys [22]. A preferential growth in the  $\langle 100 \rangle$  direction was observed in the BCC  $\beta$  phase and the long-columnar prior  $\beta$  grains of Ti-6Al-4 V [22,23] and Ti-6Al-4V-ELI [18] alloys. By controlling the crystallographic texture of the  $\beta$ -Ti-15Mo-5Zr-3Al alloy via changing the scanning strategy in SLM, the novel implants that were biocompatible and had a low Young's modulus has been successfully developed [24]. A reduction in the Young's modulus of metallic implants is important to prevent bone degradation and absorption [25]. The Young's modulus of  $\beta$ -Ti alloys strongly depends on the electron-atom (e/a) ratio, which can be controlled by manipulating the chemical composition and crystallographic orientation [24,26,27]. Thus, controlling the crystallographic texture simultaneously during the fabrication of highly dense  $\beta$ -Ti alloy components from a mixture of pure elements via SLM enables the development of novel implants with significantly low Young's modulus from alloys with a variety of compositions. The peculiar solidification

process in SLM enables the formation of a distinct solidification structure in direct-laser fabricated components; however, the control of the crystallographic structure in Ti alloys containing a single  $\beta$  phase, formed from a mixture of pure element powders has not been reported so far. In the present study, we attempted to prepare Ti alloy components using Ti-Cr, Ti-Nb, Ti-Mo, and Ti-Ta alloys, and realized the fabrication of  $\beta$ -Ti alloy components with a single  $\beta$  phase from the mixture of pure Ti and Cr powders; further, we could also control the crystallographic texture in the same time. This study demonstrates the possibility of fabricating the Ti-based alloy components with well-developed crystallographic texture from the mixture of pure elemental powders using the process of SLM, thus enhancing the affordability of titanium and its alloys.

## 2. Materials and methods

Ti<sub>80</sub>X<sub>20</sub> (X = Cr, Nb, Mo, Ta) (atomic %) alloy specimens were prepared from mixtures of the pure elemental powders in the present study. Cr, Nb, Mo, and Ta can stabilize the  $\beta$  phase in Ti; in other words, the beta transus temperature in Ti decreases by the addition of these elements. Ti powders (TILOP-45) prepared by the gas-atomizing process were supplied by Osaka Titanium Technologies Co., Ltd. The Cr powders (CRE03PB), Nb powders (NBE03PB), Mo powders (MOE09PB), and Ta powders (TAE02PB), all of which were obtained by the fracturing method, were supplied by Kojundo Chemical Laboratory Co., Ltd., Japan. Table 1 shows the median particle sizes of the pure element powders. Fig. 1 shows the scanning electron microscopy (SEM) images of the morphology of a mixture of Ti and Cr powders as a typical example of Ti<sub>80</sub>X<sub>20</sub> alloy. Detailed information on the pure element powders is summarized in the supplementary information [23]. The outer appearance of the pure element powders characterized by SEM, the particle size distribution, and their chemical composition are shown in Fig. S1, Fig. S2, and Table S1 in the supplementary information [28], respectively.

Fig. 2 illustrates the rectangular-shaped samples and the scan-strategy in the present study (Fig. 2(a)), together with the outer appearance of the alloy specimens prepared under various process conditions (Fig. 2(b)). Rectangular samples of 5 mm × 5 mm × 10 mm (building direction, Z-axis) size were manufactured by utilizing a SLM apparatus (EOS M 290, EOS, Germany) equipped with an ytterbium fiber laser in an argon atmosphere. The scan pitch was fixed at 100  $\mu$ m. The energy density (J) and the scan speed (V) were varied to investigate the optimum conditions for the fabrication of single  $\beta$ -Ti phase specimens with high density and texture control. The laser was scanned bi-directionally (zigzag) and rotated by 90° in each layer (i.e. XY-scan) in the next layer. The absolute densities of the products were measured by the Archimedes method and the relative densities of the products were calculated using the theoretical density of the mixture of pure Ti and X (X = Cr, Nb, Mo, Ta). X-ray diffraction (XRD; Philips X-pert Pro, PANalytical, Japan) analysis using Cu-K $\alpha$  radiation was carried out to identify the constituent phases and the crystallographic orientation in the prepared specimens. Electron backscattering diffraction (EBSD) analysis using a scanning electron microscope equipped with a field emission gun (FE-SEM, JSM-6500F, JEOL, Japan) was utilized to investigate the texture of the samples in detail. Table 2 lists the analysis results

**Table 1**  
Median particle size of the pure element powders.

Elements	Median size [ $\mu$ m]
Ti	23.1
Cr	18.1
Nb	13.3
Mo	12.1
Ta	9.3

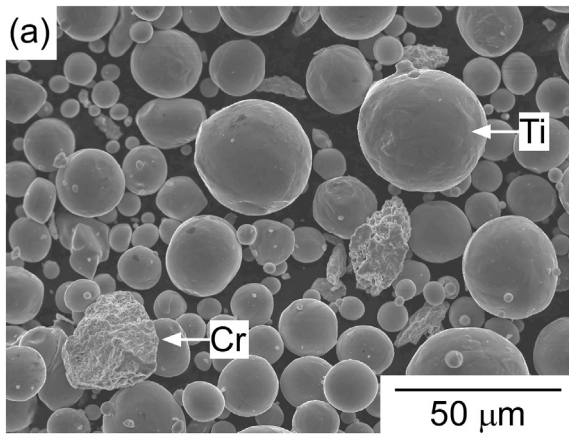


Fig. 1. SEM microstructure of the mixture of Ti and Cr powders in  $Ti_{80}Cr_{20}$  alloys.

of the chemical composition in the specimens evaluated by the SEM energy-dispersive X-ray spectroscopy (EDS). An EDS spectrum was obtained on the alloyed zone without overlapping non-molten pure metal powders into the rectangular-shaped samples under the fabrication

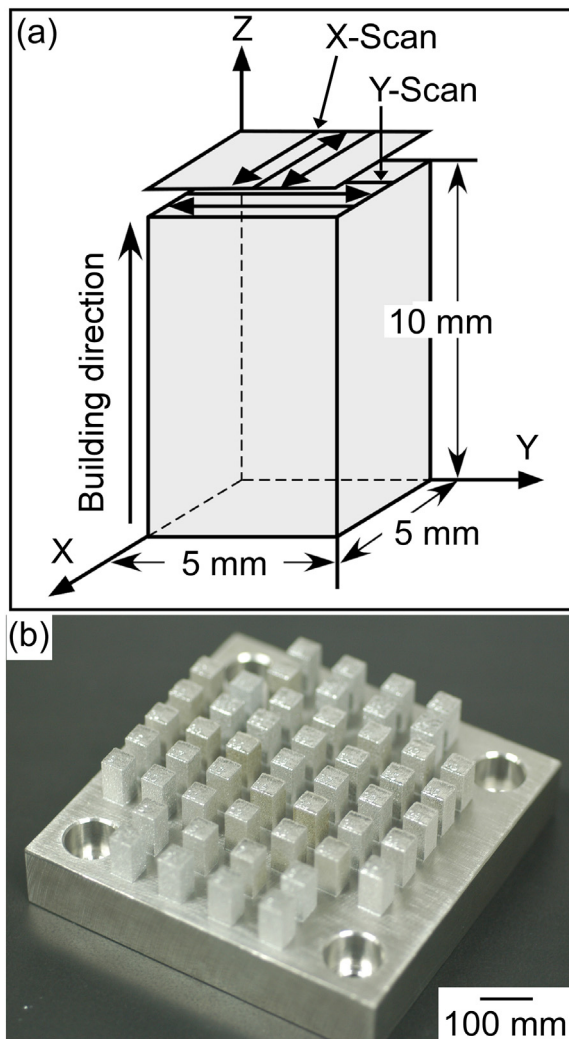


Fig. 2. Illustration of (a) the scan strategy and the Ti-Cr alloy specimens obtained from a mixture of pure Ti and Cr powders by the SLM process and (b) outer appearance of the Ti-Cr alloy samples processed under different conditions.

Table 2

The chemical composition analysis results in the specimens evaluated by the SEM-EDS, where the EDS spectrum was obtained on the alloyed zone without any non-molten pure metal powdered into the rectangular-shaped samples under appropriate fabrication conditions.

Alloys	Ti	X
Ti-Cr	82.9	17.1
Ti-Nb	80.8	19.2
Ti-Mo	79.7	20.3
Ti-Ta	80.7	19.3

condition at a scan speed  $V = 1000$  mm/s and at an energy density  $J \sim 3.0$  J/mm<sup>2</sup>. The proportion of oxygen was not evaluated in the present study. The chemical alloy composition in the alloyed zone of the specimens was similar to the nominal alloy compositions.

### 3. Results

Fig. 3 shows the XRD patterns of the Ti-X ( $X = Cr, Nb, Mo, Ta$ ) alloy specimens prepared by SLM at energy densities of 1.5 (low energy) and 3.0 (high energy) J/mm<sup>2</sup>. The XRD patterns were obtained from the Y-Z planes (Fig. 2(a)) of the specimens. The intensity is expressed in the linear scale in the figures on left and in the logarithmic scale in the figures on right, to enhance the minor peaks. The Ti-Cr alloy specimens (Fig. 3(a)) show sharp peaks corresponding to the BCC phase, regardless of the energy density in the studied condition. The Ti-Nb (Fig. 3(b)) and Ti-Ta (Fig. 3(d)) alloys exhibit peaks corresponding to the martensite ( $\alpha''$ ) and BCC phases. The peak intensity ratio between  $\alpha''$  and BCC was dependent on the energy density in the Ti-Nb and Ti-Ta alloys. The volume fraction of the  $\alpha''$  phase decreased with an increase in the energy density in Ti-Nb alloys, whereas the behavior of the Ti-Ta alloys was opposite. In the Ti-Mo alloys (Fig. 3(c)), the peak corresponding to the Mo phase can be seen together with the peak corresponding to the BCC phase of the Ti-Mo alloy. This indicates the existence of non-molten Mo particles in the Ti-Mo alloy specimens. The peak intensity corresponding non-molten Mo became weak with increasing the energy density. The above-described results clarify that the constituent phases in Ti-X1 ( $X1 = Nb, Mo, Ta$ ) alloy specimens prepared by the SLM process were strongly dependent on the element X1 and the build parameter of the SLM process. Focusing on the single BCC phase formation during the SLM process, Ti-Cr alloy system shows the high BCC single phase formation tendency at wide energy density conditions. The peak positions corresponding to the BCC phase were dependent on the energy density in the Ti-Mo (Fig. 3(c)) and Ti-Ta (Fig. 3(d)) alloys and this may be due to the change in the chemical composition of the BCC phase, which is in turn related to the amount of non-molten elemental particles. In contrast, no change in the position of the peak corresponding to the BCC phase was observed in Ti-Cr alloys (Fig. 3(a)) even when the energy density was changed. The peak intensity ratio of the BCC (011) and (002) peaks in Ti-Cr alloy specimens shows a significant energy density dependence, whereas such a dependence cannot be seen in the other Ti-X1 ( $X1 = Nb, Mo, Ta$ ) alloy specimens. This implies that the texture in the Ti-Cr alloy specimens with a single BCC phase is controllable by the SLM process. The solidification microstructure of the BCC phase in the Ti-Cr alloy specimens was investigated in detail, focusing on the formation of the texture, and the details are presented in the following sections. It should be emphasized here that various  $Ti_{80}X_{20}$  ( $X = Cr, Nb, Mo, Ta$ ) alloy specimens with the  $\beta$  phase and/or  $\alpha''$  phase can be obtained from the mixture of pure element powders. The microstructure and mechanical properties of the Ti-X1 ( $X1 = Nb, Mo, Ta$ ) alloy specimens will be discussed in future publications.

Fig. 4 shows the process window for the relative density of Ti-Cr alloy specimens prepared from a mixture of pure Ti and Cr powders via SLM, as well as the typical microstructure of the Ti-Cr alloy

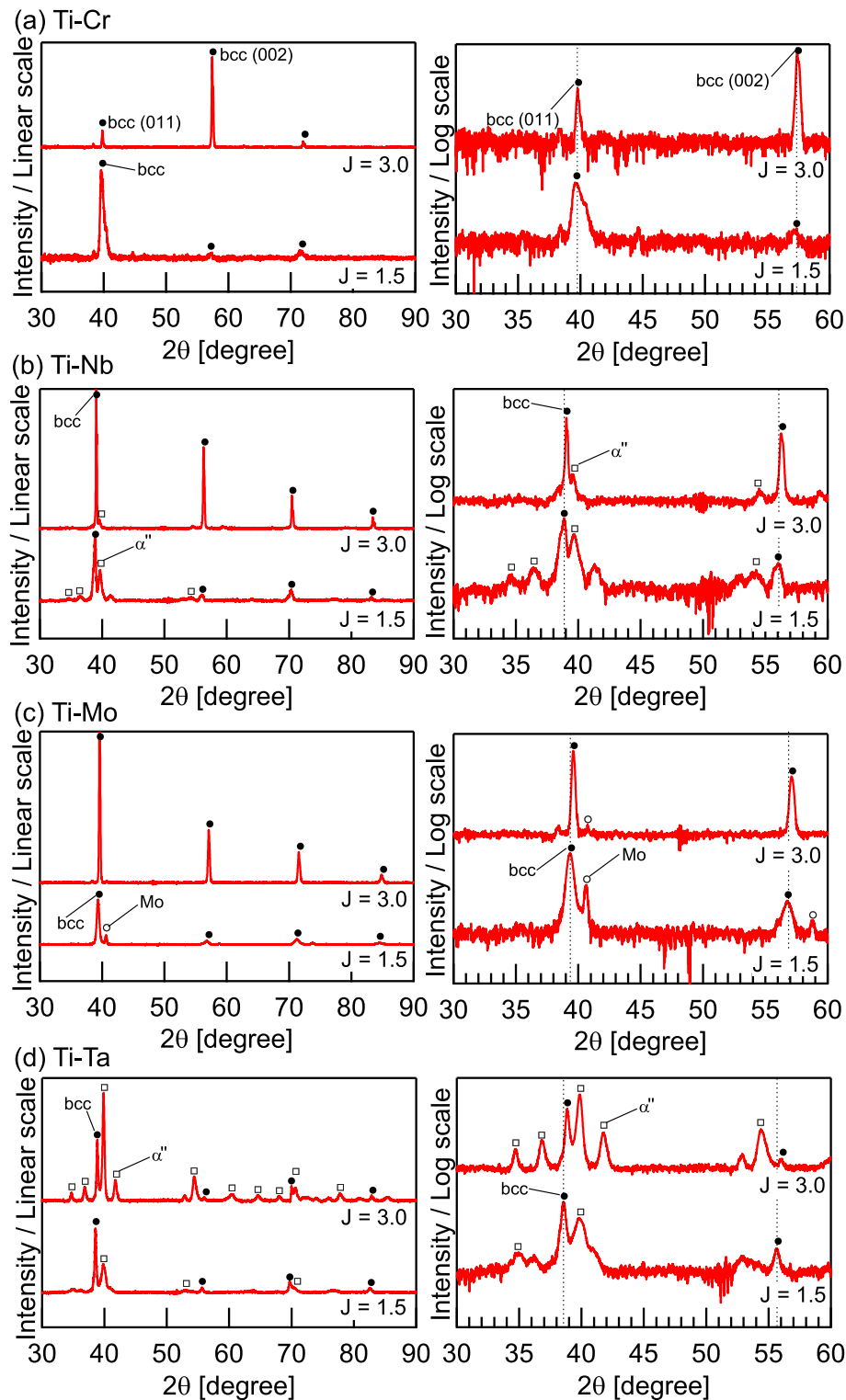


**Fig. 3.** XRD patterns of Ti-X (X = Cr, Nb, Mo, Ta) alloy specimens fabricated at energy densities ( $J$ ) of 1.5 and 3.0 J/mm<sup>2</sup>. The intensity is expressed in the linear scale in the figures on left and in the logarithmic scale in the figures on right, to enhance the minor peaks. (a) Ti-Cr alloys, (b) Ti-Nb alloys, (c) Ti-Mo alloys, and (d) Ti-Ta alloys.

specimens. In the process window map (Fig. 4(a)), the indexes ○, ●, and × denote the states with densities over 98%, between 96% and 98%, and below 96%, respectively. The hatched region including the states B, D, and E indicates suitable processing regions for achieving dense specimens without residual pores or cracks. Typical examples of the outer surface appearance of the Ti-Cr alloy specimens when the process conditions are either not suitable (A) or suitable (B) are shown in

Fig. 4(b) and (c), respectively. The black contrast corresponding to the residual pores and the non-molten Cr particles can be seen in the specimen processed under condition A (Fig. 4(b)); however, no defects could be observed in the specimen processed under condition B (Fig. 4(c)). In the specimen processed under condition A, the energy density may be too low to achieve the formation of a liquid state without non-molten Cr particles, resulting in the formation of residual pores. This



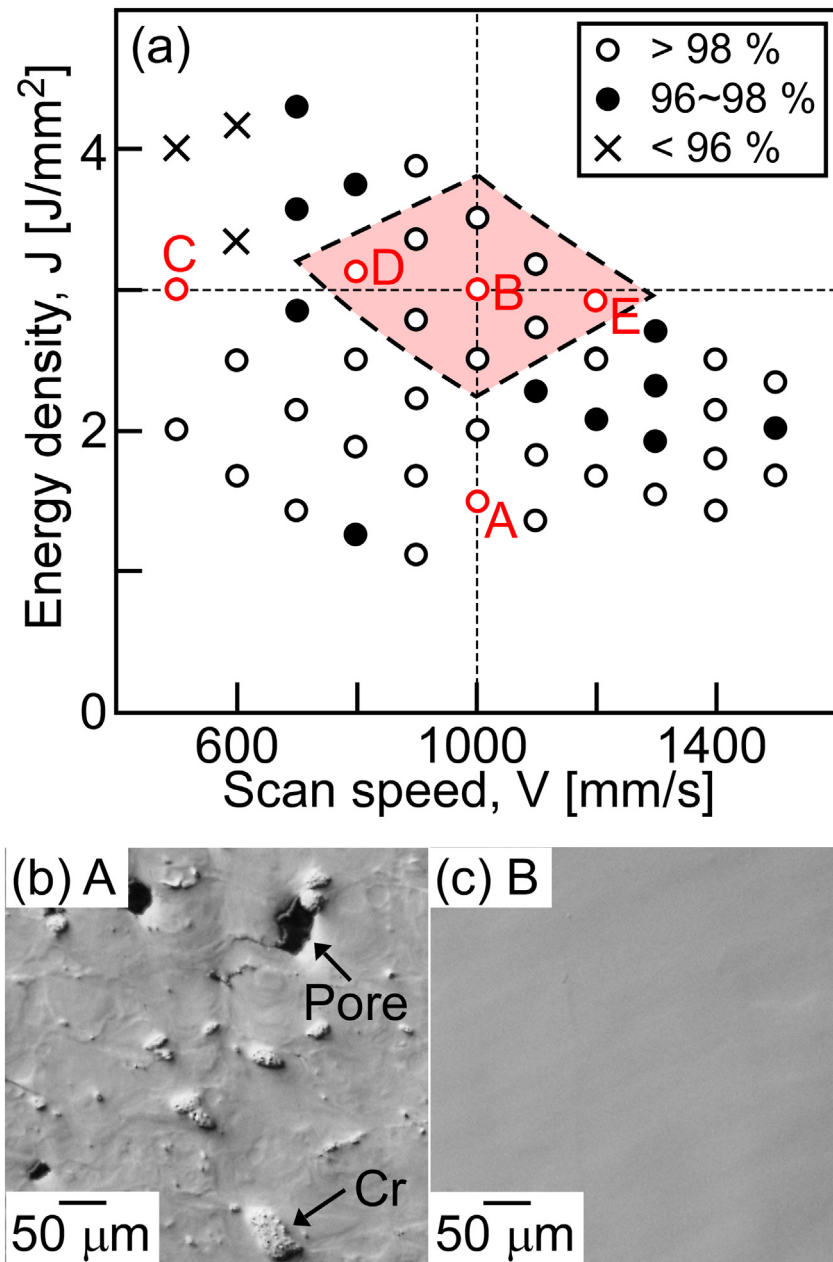


**Fig. 4.** (a) The process window map for the fabrication of Ti-Cr alloy specimens by the SLM process. A, B, C, D, and E denote the process conditions in the present study. They are as follows: (A)  $V = 1000$  mm/s,  $J = 1.5$  J/mm<sup>2</sup>, (B)  $V = 1000$  mm/s,  $J = 3.0$  J/mm<sup>2</sup>, (C)  $V = 600$  mm/s,  $J = 3.0$  J/mm<sup>2</sup>, (D)  $V = 800$  mm/s,  $J = 3.1$  J/mm<sup>2</sup>, and (E)  $V = 1200$  mm/s,  $J = 2.9$  J/mm<sup>2</sup>. (b) The outer surface appearance of the Ti-Cr alloy specimens fabricated under condition A. (c) The outer surface appearance of the Ti-Cr alloy specimens fabricated under condition B.

indicates that the microstructure is strongly dependent on the process conditions, and that an insufficient energy density leads to the formation of macroscopic defects such as the pores.

Fig. 5 shows the typical XRD patterns of Ti-Cr alloy specimens fabricated using various process conditions. Fig. 5(a) and (b) show the XRD patterns at a scan speed  $V = 1000$  mm/s and at an energy density  $J \sim 3.0$  J/mm<sup>2</sup>, respectively. The patterns were obtained from the central region of the specimens in the Y-Z planes. In Fig. 5(a) and (b), the sharp peaks indicated for the indexes ● in the XRD patterns cannot be explained by pure hcp-Ti and BCC-Cr phases. The peaks corresponding to the ● index can be ascribed to the BCC phase, whose lattice constant is  $a = 0.317$  nm. The lattice constant of the Ti<sub>80</sub>Cr<sub>20</sub> alloys, as estimated by the Vegard's law [29], is 0.317 nm. The analogy in the lattice constant value supports the formation of a BCC solid solution phase in the Ti-Cr alloy specimens under different process conditions. In the specimens

processed under condition A (Fig. 5(a)), minor peaks corresponding to the BCC-Cr phase were observed. However, the main constituent phase in the specimen processed under condition A was the BCC solid solution phase (●), while Cr is considered to be the minor phase (primarily in the non-molten particles). The BCC single phase specimens can be successfully formed from Ti-Cr alloys under different process conditions by SLM, using a mixture of pure Ti and Cr particles. One can notice that the peak intensity ratio of the (011), (002), and (112) peaks of the BCC phase is strongly dependent on the process conditions. In Fig. 5(a), the peak intensity ratio,  $I(002)/I(011)$ , increases with an increase in the energy density. In Fig. 5(b), it can be noticed that the  $I(002)/I(011)$  ratio increases with an increase in the scan velocity  $V$ . The increase in the  $I(002)/I(011)$  ratio implies the formation of a BCC solid solution phase with a high {001}<100> texture during the SLM process.

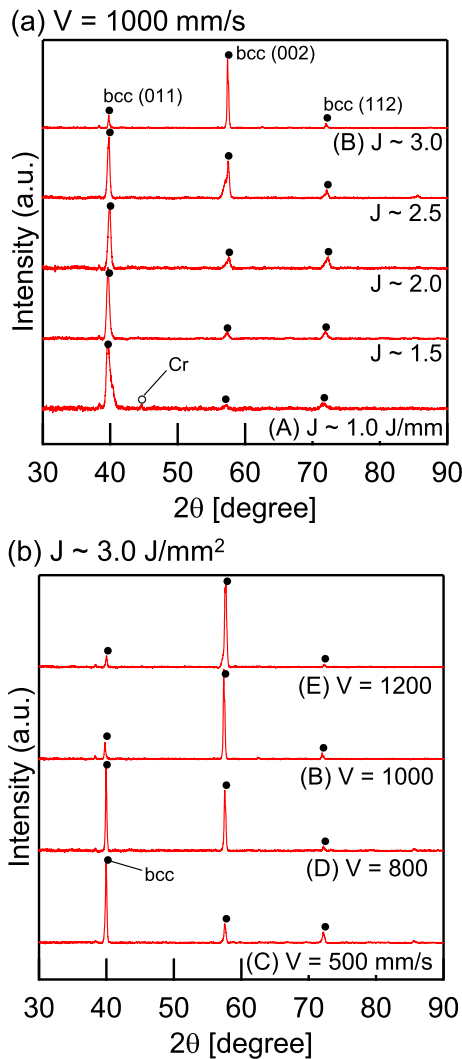


Fig. 5. XRD patterns of Ti-Cr alloy specimens processed under different SLM conditions. (a) At  $V = 1000$  mm/s and (b) at  $J \sim 3.0$  J/mm<sup>2</sup>.

To comprehend the formation of Ti-Cr alloy specimens with high texture from a mixture of pure Ti and Cr elemental powders using SLM, the microstructure of the Ti-Cr alloy specimens was investigated in detail. Fig. 6 shows the crystallographic orientation analysis results in the Y-Z plane of the Ti-Cr alloy specimens fabricated by SLM under the condition set D, in which  $V = 800$  mm/s and  $J = 3.1$  J/mm<sup>2</sup> (a), and the condition set E, in which  $V = 1200$  mm/s and  $J = 2.9$  J/mm<sup>2</sup> (b). The crystallographic orientation was evaluated by the inverse pole figure (IPF) images taken in the Y-Z planes and from the (100), (110), and (111) pole figures. Although cube (100) texture was developed in both condition D and E, a significant difference can be seen in the texture development in the specimens prepared under conditions D (Fig. 6(a)) and E (Fig. 6(b)). In the specimen E, the grains were elongated along the building direction (Z), together with a strong (001) alignment along the X direction. In contrast, few elongated grains could be seen in the Y-Z plane in the specimen D, resulting in a low (001) alignment along the X direction. Fig. 7 shows the results of the crystallographic orientation analysis along the X-Y plane of the Ti-Cr alloy specimens. No significant difference could be observed in the texture development in the specimens D (Fig. 7(a)) and E (Fig. 7(b)). Special attention must be paid to the texture in the regions indicated by R and S, the central areas of which show a strong (001) alignment, while the surrounding areas show a low crystallographic orientation. The solidification process during the SLM can explain the differences in the

crystallographic texture in the Y-Z and X-Y planes of the specimens D and E and the particular texture in the regions R and S. This will be discussed in detail in the next section. These results prove the successful fabrication of Ti-Cr alloy specimens with elongated grains in the building direction (Z), along with a high (001) alignment, from a mixture of pure Ti and Cr powders at the optimum process conditions.

#### 4. Discussion

To understand the mechanisms responsible for the development of {001}<100> crystallographic texture in the Ti-Cr alloy specimens during the SLM process, the solidification microstructures were carefully studied. Fig. 8 shows the optical microstructure of the Y-Z plane in a Ti-Cr alloy specimens prepared via SLM under process the condition set B, in which  $V = 1000$  mm/s and  $J = 3.0$  J/mm<sup>2</sup>. The polarized picture shows traces of the melt pools with a half-ellipse shape (Fig. 8(a)). The traces of the melt pools were due to the fusion processes used in this methodology. This methodology fabricates products in a track-by-track and layer-by-layer manner by partly re-melting the underlying and adjacent layers previously deposited and generating the melt pool. Fig. 8(b) shows the magnified image of the molten pools. The elongated cellular microstructure was observed from the edge of the molten pool. The traces of planar solidification, which were earlier reported by Vrancken et al. [25], could not be observed at the melt pool boundary region in the present study. Further, no non-molten elemental powders or micro-pore defects could be observed. The single Ti-Cr alloy liquid phase was obtained during the laser melting process, and rapid solidification led to the formation of the cellular microstructure. In the present study, dendrite formation and planar growth interface were not observed in the Ti-Cr alloy specimens, regardless of the process conditions. The solidification in alloys is well known to be dependent on the growth rate,  $V_c$ , which is related to the cooling rate [26]. The solidification mode changes from dendrite growth to cell growth to planar growth upon increasing the  $V_c$  (or cooling rate) during the conventional and rapid solidification processes. This indicates that a change in the scan speed,  $V$ , was not enough to change the solidification mode.

The solidification microstructure in the Ti-Cr alloy specimens prepared by the SLM at an energy density  $J \sim 3.0$  J/mm<sup>2</sup> was evaluated in detail to analyze the formation of the (001) texture. The results are shown in Fig. 9. The intensity ratio,  $I$  (Fig. 9(a)), and the grain size and the cell spacing (Fig. 9(b)) were evaluated in the Y-Z planes of the specimens. The grain size was defined as the length of the long axis in the elongated grains (Z direction). To quantitatively evaluate the degree of alignment in the (001) direction in the Ti-Cr alloy specimens, the value of the intensity ratio,  $I$ , was calculated using Eq. (1):

$$I = \frac{I_{002}}{I_{002} + I_{011}} \quad (1)$$

where  $I_{002}$  and  $I_{011}$  are the X-ray diffraction peak integral intensities of the (002) and (110) planes of the BCC solid solution phase shown in Fig. 5(b). The higher the value of  $I$ , the higher is the degree of the (001) orientation. The intensity ratio strongly depended on the scan speed  $V$  (Fig. 9(a)); an increase in the scan speed led to an increase in the (001) orientation ( $C \rightarrow D \rightarrow B \rightarrow E$ ). As can be seen in Fig. 9(b), the cell spacing increased monotonously with increasing scan speed. The cell spacing,  $\lambda$ , is then calculated using the following equation (Eq. (2)):

$$\lambda = \frac{4.3(\Delta T_0 D \Gamma)}{k^{0.25} V_c^{0.25} G^{0.25}} \quad (2)$$

where  $\Delta T_0$  is the liquidus-solidus range,  $D$  is the diffusion coefficient of the liquid,  $\Gamma$  is the Gibbs-Thomson coefficient,  $k$  is the equilibrium distribution coefficient,  $V_c$  is the growth rate, and  $G$  is the interface temperature gradient [30]. The change in the cell spacing can be explained by the change in  $V_c$  and/or  $G$ . The cell spacing in the specimen E ( $V =$

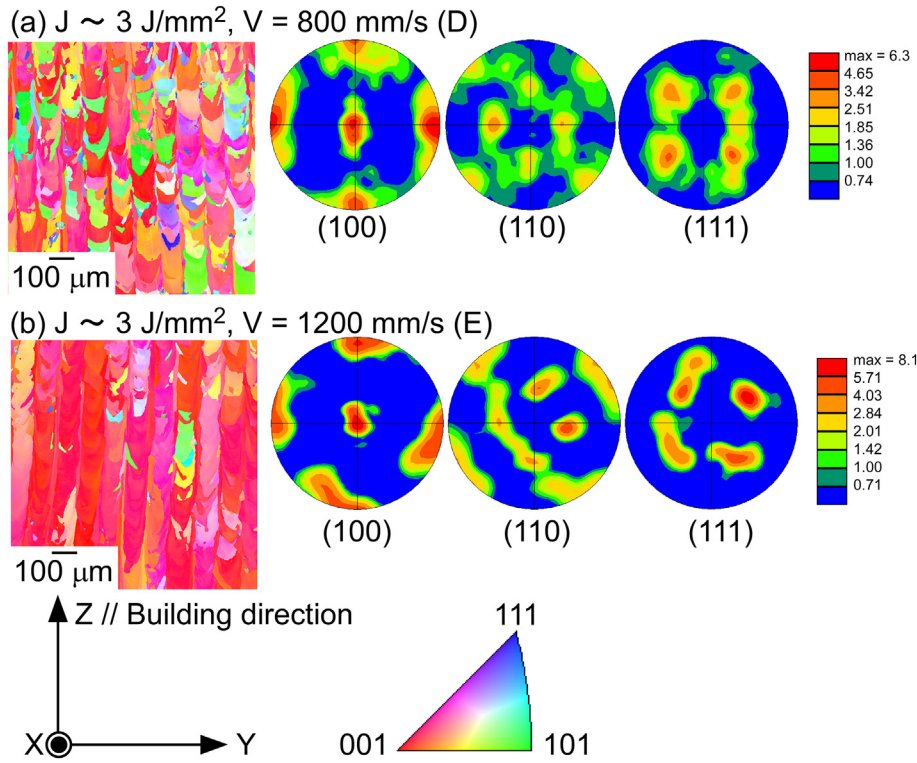


**Fig. 6.** Crystallographic orientation analysis of the Y-Z plane in the Ti-Cr alloy specimens fabricated by SLM under (a) condition D ( $V = 800 \text{ mm/s}$ ,  $J = 3.1 \text{ J/mm}^2$ ) and (b) condition E ( $V = 1200 \text{ mm/s}$ ,  $J = 2.9 \text{ J/mm}^2$ ). Crystallographic orientation was evaluated by the IPF images captured in the Y-Z planes and the (100), (110), and (111) pole figures.

1200 mm/s) is about 1.4 times larger than that in the specimen C ( $V = 500 \text{ mm/s}$ ). If the cell spacing was changed only by the variation of  $V_C$  while maintaining a constant  $G$  (the assumption of a constant  $G$  is

roughly derived from the constant energy density  $J$ ), the  $V_C$  of the specimen E ( $V = 1200 \text{ mm/s}$ ) could be roughly estimated to be one-fourth the  $V_C$  of the specimen C ( $V = 500 \text{ mm/s}$ ). The decrease in the cell

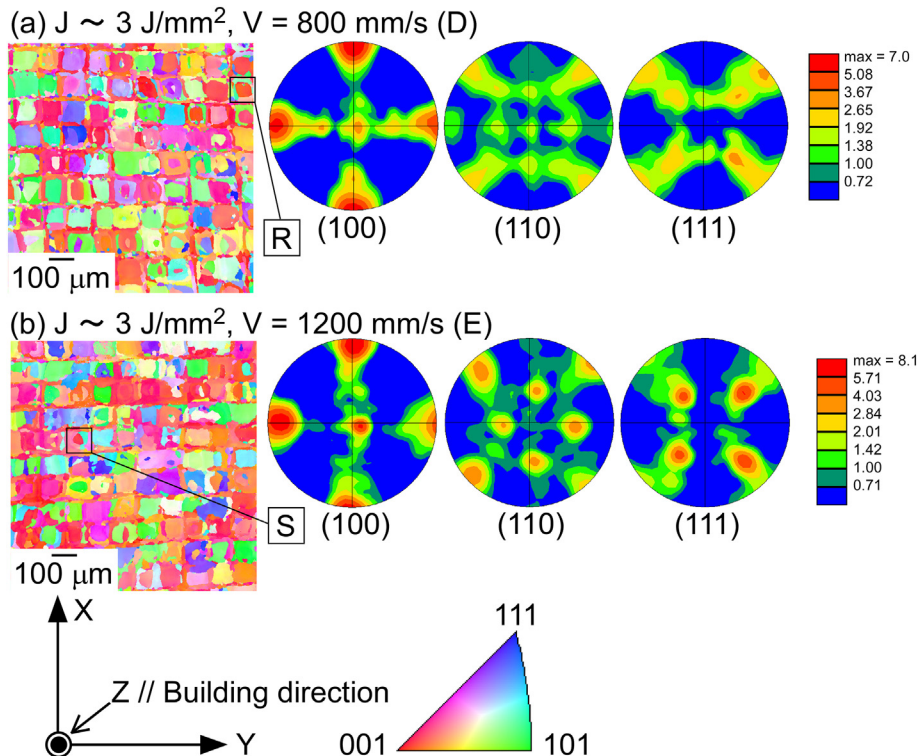


**Fig. 7.** Crystallographic orientation analysis results of the X-Y plane in the Ti-Cr alloy specimens fabricated by SLM under (a) condition D ( $V = 800 \text{ mm/s}$ ,  $J = 3.1 \text{ J/mm}^2$ ) and (b) condition E ( $V = 1200 \text{ mm/s}$ ,  $J = 2.9 \text{ J/mm}^2$ ). Crystallographic orientation was evaluated by the IPF images captured in the X-Y planes and the (100), (110), and (111) pole figures.



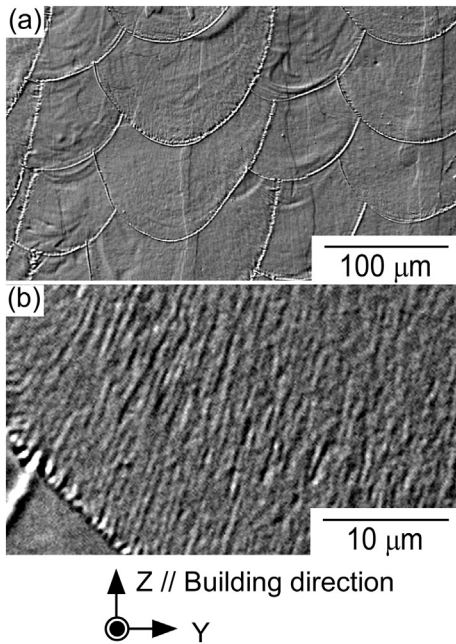


**Fig. 8.** Optical microstructure of the Y-Z plane in the Ti-Cr alloy specimens fabricated by SLM under condition B ( $V = 1000$  mm/s,  $J = 3.0$  J/mm<sup>2</sup>). (a) Magnified microstructure focusing on the shell structure formation, (b) magnified microstructure of the region P in Fig. 7(a), and (c) magnified microstructure of the region Q in Fig. 7(a).

spacing indicates a decrease in the  $V_C$ ; the low  $V_C$  can be considered to be favorable for high crystallographic orientation in the solidified grains. One can notice that the increase in the grain size corresponds to an

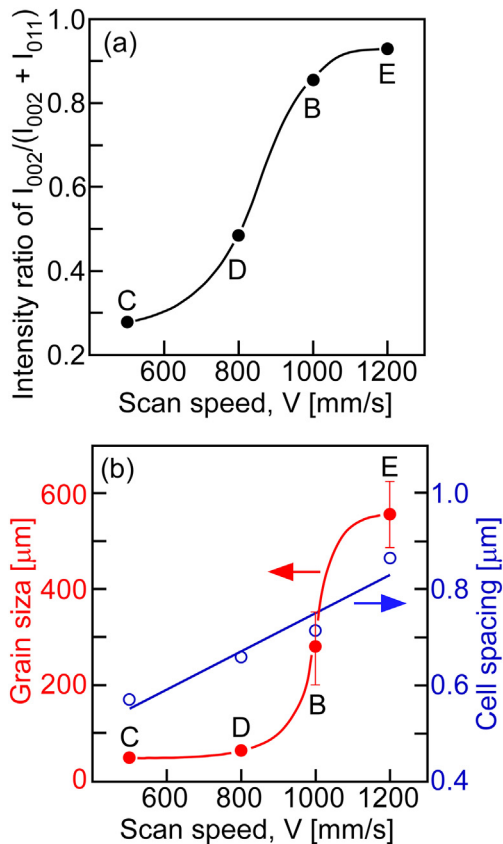


**Fig. 9.** Solidification microstructure analysis of the Ti-Cr alloy specimens fabricated by SLM at  $J \sim 3.0$  J/mm<sup>2</sup>.

increase in the intensity ratio. The increase in the grain size also led to the formation of highly oriented grains during the SLM process because of the epitaxial crystal growth from the previously solidified parts. The re-melting of the previously solidified Ti-Cr alloy layers and the epitaxial growth of the Ti-Cr alloy grains with a  $\langle 001 \rangle$  orientation, based on the previously solidified grains with a  $\langle 001 \rangle$  orientation, can lead to the formation of elongated grains with a high  $\langle 001 \rangle$  orientation. The change in the scan speed is not enough to change the solidification mode from cell growth to other growth modes. However, it was enough to change the  $V_C$  during the solidification process, resulting in a low  $V_C$  and/or  $G$  and enhancing the formation of elongated grains with a high  $\langle 001 \rangle$  orientation.

The strong  $\langle 001 \rangle$  texture formation can be seen in the elongated grains in the Y-Z plane of the Ti-Cr alloy specimens (Fig. 6) under

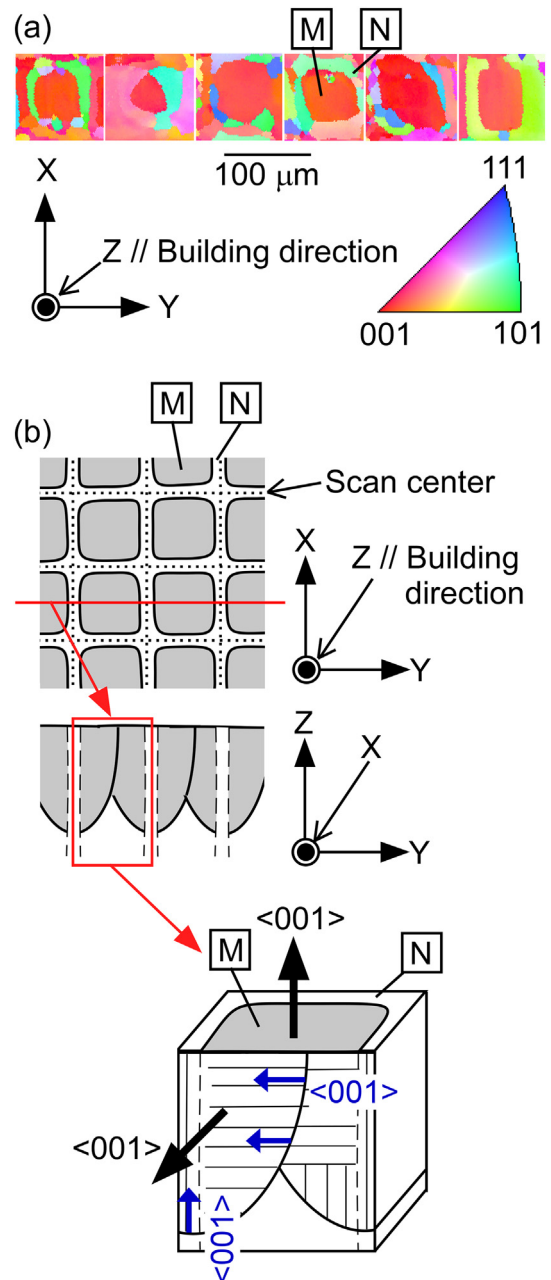


**Fig. 10.** Illustration of the crystallographic orientation in the X-Y planes during SLM. (a) Typical examples of the molten pools with a highly oriented central area (M) and surrounding areas with a low orientation. (b) Mechanism of texture evolution during the SLM process.



specific conditions, whereas it could not be observed in the X-Y plane (Fig. 7). It is well known that the preferred orientation for dendritic and cell growth in metals with a BCC structure is  $\langle 001 \rangle$  [30–32]. The texture formation is related to the preferred orientation of growth of the BCC structure, the solidification mode as described earlier, the thermal gradient during the SLM process, and other related factors. Fig. 10 depicts the particular crystallographic texture at the trace of the melt pools in the X-Y plane and illustrates the mechanism of texture formation in the X-Y and Y-Z planes. Fig. 10(a) shows six examples of texture formation at the traces of the melt pools in the X-Y plane, corresponding to the regions indicated by R and S in Fig. 7. The central area (indicated by M) shows a significantly high  $\langle 001 \rangle$  texture, which is not visible in the surrounding regions (indicated by N). Ishimoto et al. reported the mechanism of the  $\langle 001 \rangle$  texture formation during the fabrication process with scan strategy XY in  $\beta$ -Ti alloys, and a part of the illustration for the same is provided in Fig. 10(b) [24]. The  $\langle 001 \rangle$  is preferentially oriented along the building direction, which is caused by the two  $\langle 001 \rangle$  epitaxial growth directions that are  $0^\circ$  and  $90^\circ$  from the building direction. The region N with a low  $\langle 001 \rangle$  texture corresponds to the elongated grain along the building direction. One can notice the difference in the  $\langle 001 \rangle$  texture formation between the regions M and N. In the region N, the heat flow is directed favorably towards the  $\langle 001 \rangle$  direction in the BCC phase and the epitaxial growth occurs. In contrast, in the region M, the growth of the elongated cell predominantly occurs within the plane that is perpendicular to the scanning direction. The region N corresponds to the scan center during the SLM process. The solidification progressed along the interface between the boundaries of the molten pool, indicating that the region N solidified towards the end of the process. This implies that the solidification in the region N was affected by that in the region M, and this effect may lead to a low degree of texture formation. The difference in the  $\langle 001 \rangle$  texture formation between the X-Y and Y-Z planes can be explained by the preferred orientation of cell growth in metals with a BCC structure and the particular texture formation mechanism is related to the heat transfer during the SLM process. The mixture of the regions M and N is the reason why no significant  $\langle 001 \rangle$  texture formation could be seen in the X-Y plane when compared with the Y-Z plane. The heat transfer in the melt and the solidification interface between the liquid and solid during the SLM process have not been studied in detail in the current work. The combination of the simulation of heat transfer during the SLM process and the microstructure analysis, as performed in the present study, may be effective in furthering our understanding of crystallographic orientation in pure Ti and Ti alloys. The crystallographic texture formation was found in the Ti-Cr alloy system, while such a phenomenon was not be clearly observed in Ti-X1 ( $X_1 = \text{Nb, Mo, Ta}$ ) alloy specimens, as shown in Fig. 3. The single  $\beta$  phase was obtained regardless of the process conditions in Ti-Cr alloys, while the martensite phase and non-molten phase were observed in Ti-X1 ( $X_1 = \text{Nb, Mo, Ta}$ ) alloy specimens. These factors observed only in Ti-X1 ( $X_1 = \text{Nb, Mo, Ta}$ ) alloys may affect the crystallographic texture formation. The development of crystallographic texture in Ti-based alloy components without any non-molten particles and macroscopic defects was considered to affect the mechanical properties, and the relationship between the mechanical properties and the solidification microstructure will be reported in the future work. The present study demonstrates the possibility of fabrication of the  $\beta$ -Ti alloy components containing a well-developed crystallographic texture from a mixture of pure metallic elemental powders in Ti-Cr alloys, which consist of spherical Ti powders and irregularly shaped Cr powders, using additive manufacturing.

## 5. Conclusions

In this study, the dense components of the Ti-X ( $X = \text{Cr, Nb, Mo, Ta}$ ) alloy specimens were fabricated from the mixtures of pure element powders using an SLM process. The constituent phases in the dense components of the Ti-X alloys were evaluated. The formation of a single

$\beta$  phase without non-molten powders was observed in these alloys. Based on the solidification microstructure analysis of Ti-Cr alloys, the texture formation and its mechanism were investigated. The obtained results are summarized as follows:

- (1) The formation of a BCC phase was observed in  $\text{Ti}_{80}\text{X}_{20}$  ( $X = \text{Cr, Nb, Mo, Ta}$ ) alloys prepared using a mixture of pure element powders processed by the SLM technique. The constituent phases (BCC phase, martensite phase, and non-molten pure element phase, etc.) and the volume fraction of the constituent phases were dependent on the element X and the energy density during the SLM process.
- (2) The dense components of a single  $\beta$  phase Ti-Cr alloys without non-molten powders was fabricated from a mixture of pure Ti and Cr powders using the process of SLM.
- (3) The crystallographic texture of the  $\beta$  phase in the Ti-Cr alloy specimens was analyzed. The preferential  $\{001\}\{100\}$  crystallographic orientation and the formation of elongated grains along the building direction were observed.
- (4) The mechanism of formation of with well-developed  $\{001\}\{100\}$  crystallographic texture was discussed based on the formation of the elongated grains, the epitaxial growth of the previously solidified layer, cell growth at the solid-liquid interface, and the heat transfer and solidification processes during SLM. The change in the crystallographic orientation of the  $\beta$  phase cannot be explained by a change in the solidification mode.

## CRediT authorship contribution statement

**Takeshi Nagase:** Writing - original draft. **Takao Hori:** Investigation. **Mitsuharu Todai:** Investigation. **Shi-Hai Sun:** Investigation. **Takayoshi Nakano:** Project administration.

## Acknowledgements

This work was supported by the Council for Science, Technology and Innovation (CSTI), the Cross-Ministerial Strategic Innovation Promotion Program (SIP), and Innovative design/manufacturing technologies (Establishment and Validation of the Base for 3D Design & Additive Manufacturing Standing on the Concepts of Anisotropy & Customization) from the New Energy and Industrial Technology Development Organization (NEDO).

This work was also supported by Grants-in-Aid for Scientific Research from the Japan Society for the Promotion of Science (grant number: 18H05254, 25220912).

## Appendix A. Supplementary data

Supplementary data to this article can be found online at <https://doi.org/10.1016/j.matdes.2019.107771>.

## References

- [1] D. Banerjee, J.C. Williams, Perspectives on titanium science and technology, *Acta Mater.* 61 (2013) 844–879.
- [2] M. Geetha, A.K. Singh, R. Asokamani, A.K. Gogia, Ti based biomaterials, the ultimate choice for orthopaedic implants - a review, *Prog. Mater. Sci.* 54 (2009) 309–426.
- [3] C.K. Chua, K.F. Leong, *Rapid Prototyping: Principles and Applications in Manufacturing*, Wiley, New York, 1997.
- [4] J. Beaman, J.W. Barlow, D.L. Bourell, R.H. Crawford, H.L. Marcus, K.P. McAlea, *Solid Freeform Fabrication: A New Direction in Manufacturing*, Kluwer Academic Publishers, Dordrecht, 1997.
- [5] L. Lu, J. Fuh, Y.S. Wong, *Laser Induced Materials and Processes for Rapid Prototyping*, Kluwer Academic Publishers, Dordrecht, 2001.
- [6] M. Shellabear, J. Lenz, V. Junior, E-manufacturing with laser sintering-to series production and beyond, in: *Proceedings of the Fourth Laser Assisted Net Shape Engineering, LANE 2004*, Vol. 1, September, Erlangen, Germany, pp. 435–444.
- [7] T. Wohlers, *Wohlers Report, Rapid Prototyping and Tooling State of the Industry*, Wohlers Associates, 2002.

- [8] E.C. Santos, M. Shiomi, K. Osakada, T. Laoui, Rapid manufacturing of metal components by laser forming, *Int. J. Mach. Tools Manuf.* 46 (2006) 1459–1468.
- [9] K. Hagihara, T. Nakano, M. Suzuki, T. Ishimoto, Suyalatu, S.H. Sun, Successful additive manufacturing of MoSi<sub>2</sub> including crystallographic texture and shape control, *J. Alloys Compd.* 696 (2017) 67–72.
- [10] M. Todai, T. Nakano, T. Liu, H.Y. Yasuda, K. Hagihara, K. Cho, M. Ueda, M. Takeyama, Effect of building direction on the microstructure and tensile properties of Ti-48Al-2Cr-2Nb alloy additively manufactured by electron beam melting, *Addit. Manuf.* 13 (2017) 61–70.
- [11] S.L. Sing, W.Y. Yeong, F.E. Wiria, Selective laser melting of titanium alloy with 50 wt% tantalum: microstructure and mechanical properties, *J. Alloys Compd.* 660 (2016) 461–470.
- [12] H. Schwab, F. Palm, U. Kühn, J. Eckert, Microstructure and mechanical properties of the near-beta titanium alloy Ti-5553 processed by selective laser melting, *Mater. Des.* 105 (2016) 75–80.
- [13] B. AlMangour, D. Grzesiak, T. Borkar, J.M. Yang, Densification behavior, microstructural evolution, and mechanical properties of TiC/316L stainless steel nanocomposites fabricated by selective laser melting, *Mater. Des.* 138 (2018) 119–128.
- [14] B. AlMangour, M.S. Baek, D. Grzesiak, K.A. Lee, Strengthening of stainless steel by titanium carbide addition and grain refinement during selective laser melting, *Mater. Sci. Eng. A* 712 (2018) 812–818.
- [15] T. Hua, C. Jing, Z. Fengying, L. Xin, H. Weidong, Microstructure and mechanical properties of laser solid formed Ti-6Al-4V from blended elemental powders, *Rare Metal Mater. Eng.* 38 (2009) 574–578.
- [16] P.C. Collins, R. Banerjee, S. Banerjee, H.L. Fraser, Laser deposition of compositionally graded titanium/vanadium and titanium/molybdenum alloys, *Mater. Sci. Eng. A* 352 (2003) 118–128.
- [17] A. Almeida, D. Gupta, C. Loable, R. Vilar, Laser-assisted synthesis of Ti-Mo alloys for biomedical applications, *Mater. Sci. Eng. C* 32 (2012) 1190–1195.
- [18] B. Vrancken, L. Thijs, J.P. Kruth, J. Van Humbeeck, Microstructure and mechanical properties of a novel  $\beta$  titanium metallic composite by selective laser melting, *Acta Mater.* 68 (2014) 150–158.
- [19] M. Ficher, D. Jought, G. Robin, L. Peltier, P. Laheurte, In situ elaboration of a binary Ti-26Nb alloy by selective laser melting of elemental titanium and niobium mixed powders, *Mater. Sci. Eng. C* 62 (2016) 852–859.
- [20] L. Yan, Y. Yuan, L. Ouyang, H. Li, A. Mirzasadeghi, L. Li, Improved mechanical properties of the new Ti-15Ta-xZr alloys fabricated by selective laser melting for biomedical application, *J. Alloys Compd.* 688 (2016) 156–162.
- [21] M. Todai, T. Nagase, T. Hori, H. Motoki, S.H. Sun, K. Hagihara, T. Nakano, Fabrication of the beta-titanium alloy rods from a mixture of pure metallic element powders via selected laser melting, *Mater. Sci. Forum* 941 (2018) 1260–1263.
- [22] L. Thijs, F. Verhaeghe, T. Craeghs, J. Van Humbeeck, J.P. Kruth, A study of the microstructural evolution during selective laser melting of Ti-6Al-4V, *Acta Mater.* 58 (2010) 3303–3312.
- [23] P.A. Kobryn, S.L. Semiatin, Microstructure and texture evolution during solidification processing of Ti-6Al-4V, *J. Mater. Process. Technol.* 135 (2003) 330–339.
- [24] T. Ishimoto, K. Hagihara, K. Hisamoto, S.H. Sun, T. Nakano, Crystallographic texture control of beta-type Ti-15Mo-5Zr-3Al alloy by selective laser melting for the development of novel implants with a biocompatible low Young's modulus, *Scr. Mater.* 132 (2017) 34–38.
- [25] Y. Noyama, T. Miura, T. Ishimoto, T. Itaya, M. Niinomi, T. Nakano, Bone loss and reduced bone quality of the human femur after total hip arthroplasty under stress-shielding effects by titanium-based implant, *Mater. Trans.* 53 (2012) 565–570.
- [26] M. Tane, S. Akita, T. Nakano, K. Hagihara, Y. Umakoshi, M. Niinomi, H. Nakajima, Peculiar elastic behavior of Ti-Nb-Ta-Zr single crystals, *Acta Mater.* 56 (2008) 2856–2863.
- [27] S.H. Lee, M. Todai, M. Tane, K. Hagihara, H. Nakajima, T. Nakano, Biocompatible low Young's modulus achieved by strong crystallographic elastic anisotropy in Ti-15Mo-5Zr-3Al alloy single crystal, *J. Mech. Behav. Biomed. Mater.* 14 (2012) 48–54.
- [28] See the supplementary materials.
- [29] L. Vegard, Die Konstitution der Mischkristalle und die Raumfüllung der Atome, *Z. Physiother.* 5 (1921) 17–26.
- [30] W. Kurz, D.J. Fisher, *Fundamentals of Solidification*, Trans Tech Publications, 1998.
- [31] B. Chalmers, *Principles of Solidification*, John Wiley and Sons, 1964.
- [32] W.C. Winegard, *An Introduction to the Solidification of Metals*, The Institute of Metals, London, 1964.